Electrochemically Synthesized Liquid–Sulfur/Sulfide Composite Materials for High-Rate Magnesium Battery Cathodes

SCHOLARONE™
Manuscripts

ARTICLE

Electrochemically Synthesized Liquid-Sulfur/Sulfide Composite Materials for High-Rate Magnesium Battery Cathodes

Kohei Shimokawa*[a,b], Takuya Furuhashi[a], Tomoya Kawaguchi[a], Won-Young Park[a], Takeshi Wada[a], Hajime Matsumoto[c], Hidemi Kato[a], Tetsu Ichitsubo*[a]

Mg/S battery is one of the most promising rechargeable batteries owing to its high theoretical energy density. The development is, however, hindered by (i) low electronic conductivity of S, (ii) sluggish Mg^{2+} diffusion in solid Mg–S compounds formed by discharge, and (iii) dissolubility of polysulfides into electrolytes. To address these problems, we propose liquid-S/sulfide composite cathode materials in combination with an ionic liquid electrolyte at intermediate temperatures (~150°C). The composite structure is spontaneously fabricated by electrochemically oxidizing metal sulfides, yielding liquid S embedded in a porous metal-sulfide conductive frame. This concept is demonstrated by a S/FeS_2 composite cathode, which shows a significantly high-rate capability of, e.g., 1246 $mA/g_{(S)}$ with a capacity of ~900 $mAh/g_{(S)}$. In addition, non-equilibrium liquid S formed by fast charging results in an unexpected higher discharge potential. This work provides a new strategy to design S-based cathodes for achieving high-rate multivalent rechargeable batteries.

Introduction

Over the decades, Li-ion batteries (LIBs) have dramatically improved the convenience of our daily lives. However, there remain big challenges in terms of elemental resources and safe operation, especially for the relatively large-scale applications (e.g., electric vehicles and stationary energy storage systems). Thus, the next step in battery science is establishing ecologically-friendly multivalent batteries using abundant elements such as Mg, Zn, and Al [1]. Mg rechargeable batteries (MRBs) are one of the most promising candidates for next-generation batteries thanks to the following advantages of Mg metal anode. (i) Mg metal tends to smoothly deposit without dangerous dendritic growth [2,3]. (ii) Mg metal has a largely negative electrode potential (–2.38 V vs. SHE) and a high specific capacity (3833 mAh/cm^3). (iii) Mg is a naturally abundant, low cost, and non-toxic element.

In contrast to the great advantages of Mg metal anode, there are few reports of cathode materials showing stable battery performance [4–7], which is the main bottleneck in developing MRBs. In 2000, Aurbach et al. reported the first prototype system of MRBs with Mo_6S_8 cathode [4], which shows excellent cycle performance at room temperature, whereas relatively low potential (~1.1 V vs. Mg^{2+}/Mg) and capacity (~100

mAh/g) limit the energy density of the whole battery. Recently, the capacity was greatly improved to 150–200 mAh/g by using TiS_2 and TiO_2-based materials [5,6] while the redox potentials are as low as 1.0–1.5 V vs. Mg^{2+}/Mg. Consequently, their energy densities with Mg-metal anode are approximately 200 Wh/kg, which is still lower than that of conventional LIBs (cf. ~370 Wh/kg for $LiCoO_2$/C cells). To increase the redox potential of cathode materials, it would be promising to utilize metal oxides containing later transition metals such as Cr, Mn, Fe, and Co by analogy with LIBs. Indeed, our group has reported the feasibility of 2–3 V class cathode materials for MRBs with spinel-type structures with later transition metals [8–13], but the sluggish diffusion of Mg^{2+} hampers both the current density and capacity of the oxide cathodes. For instance, the former typically ranges 10–20 mA/g even at the temperature of 150°C, and the latter is practically limited to 100–200 mAh/g.

Sulfur (S) cathode has been attracting much attention [14–29] to circumvent the inherent problems in intercalation materials for MRBs. The most remarkable point of the S cathode is its extremely high theoretical energy density, which amounts to ~1700 Wh/kg owing to the high capacity of 1672 mAh/g and the moderate average potential of ~1.77 V vs. Mg^{2+}/Mg [16,23,24]. Since Muldoon et al. demonstrated the feasibility of Mg/S battery in 2011 [14], many efforts have been devoted to improving the battery performances by designing electrolytes [14–16,19,21,23,27], architecture of S/carbon nanocomposites [17,18,24], and functional separator or interlayer [17,26,28,29]. It is, however, still challenging to achieve high-rate capabilities because of low electronic conductivity of S and sluggish Mg^{2+} diffusion in solid Mg–S compounds formed by discharge [15,20,22], which often results in poor reversibility due to the large polarization of the electrode. In addition, complicated fabrication processes of the composite electrodes are

[a.] Institute for Materials Research, Tohoku University, 2-1-1 Katahira, Aoba-ku, Sendai 980-8577, Japan. E-mail: kohei.shimokawa.b7@tohoku.ac.jp; tichi@imr.tohoku.ac.jp

[b.] Frontier Research Institute for Interdisciplinary Sciences, Tohoku University, 6-3 Aramaki Aza Aoba, Aoba-ku, Sendai 980-8578, Japan.

[c.] Research Institute of Electrochemical Energy, National Institute of Advanced Industrial Science and Technology (AIST), 1-8-31, Midorigaoka, Ikeda, Osaka 563-8577, Japan

disadvantageous for practical use. Therefore, a simple method to enhance the reaction kinetics is strongly demanded for exploiting the S cathode.

In this work, we propose electrochemically synthesized liquid-S/sulfide composite materials, realizing high-rate Mg–S batteries that can work at intermediate temperatures around 150°C. The composite materials are spontaneously formed by simply charging metal sulfides (*M*S), which results in the following reactions (see Figure 1a). Metal cations (*M*$^{n+}$) are electrochemically extracted from *M*S particles in an ionic liquid electrolyte that hardly dissolves S. This yields elemental S, active material, embedded in the *M*S conductive frame to form the composite structure. The elemental S melts in this composite because the operating temperature of 150°C is above its melting point (~120°C) [18,30], which enhances the reaction kinetics by utilizing liquid state reaction. The *M*S host plays a role in adsorbing polysulfides and assuring sufficient electron conductivity during charge/discharge [31–33], which is a great advantage compared to carbon-based host materials while the weight is a drawback. In this manner, the formed composite materials can work as cathodes for high-rate MRBs. Although the elevated temperature operation is not suitable for mobile devices, it is acceptable for relatively large-scale batteries, which are strongly required for electric vehicles and smart grids. Actually, Na/S batteries operated at ~300°C are used as large-scale energy storage systems, but the liquid Na used as the anode is hazardous. In contrast, the operation temperature of 150°C applied in this work is much lower than the melting point of Mg metal, enabling safe operation.

Results and discussion

FeS$_2$ was chosen as a starting material to exemplify the concept of this study due to the following reasons. (i) FeS$_2$ shows a relatively high electric conductivity, known as a famous narrow-gap (~0.95 eV) semiconductor [34]. (ii) FeS$_2$ has the pyrite structure consisting of Fe and S–S dumbbells as depicted in Figure S1; thus, it is expected that Fe^{2+} cations are easily extracted from FeS$_2$ because of the low electrostatic interaction with S$_2^{2-}$ having low negative charge density. (iii) FeS$_2$ is an earth-abundant and non-toxic mineral, which is advantageous for achieving cost-effective and environmentally-friendly batteries. Electrodes were prepared by mixing FeS$_2$ particles, whose diameter ranges 1–20 mm (Figure S2), carbon black, and polyvinylidene fluoride (PVdF) binder in a weight ratio of 8:1:1 and then courting it on a Pt foil. Electrochemical experiments were performed at 150°C using a three-electrode beaker-type cell with an ionic liquid electrolyte of (Mg10/Cs90)TFSA [35] (TFSA: bis(trifluoromethanesulfonyl)amide), where CsTFSA was mixed with Mg(TFSA)$_2$ to decrease the melting point. Note that TFSA-based ionic liquids reportedly suppress the dissolution of polysulfides owing to their weak donor ability [36–38]. Besides, the excellent oxidative stability of (Mg10/Cs90)TFSA up to ~5 V vs. Li$^+$/Li [8,9] enables us to synthesize the aforementioned composite electrode at relatively high potentials. Because Mg metal is readily passivated in the electrolyte due to the decomposition and/or adsorption of TFSA anions on it [39–41], a Li-based system (denoted as Li RE; see Figure S3) was used as the reference electrode. It was employed in our previous works
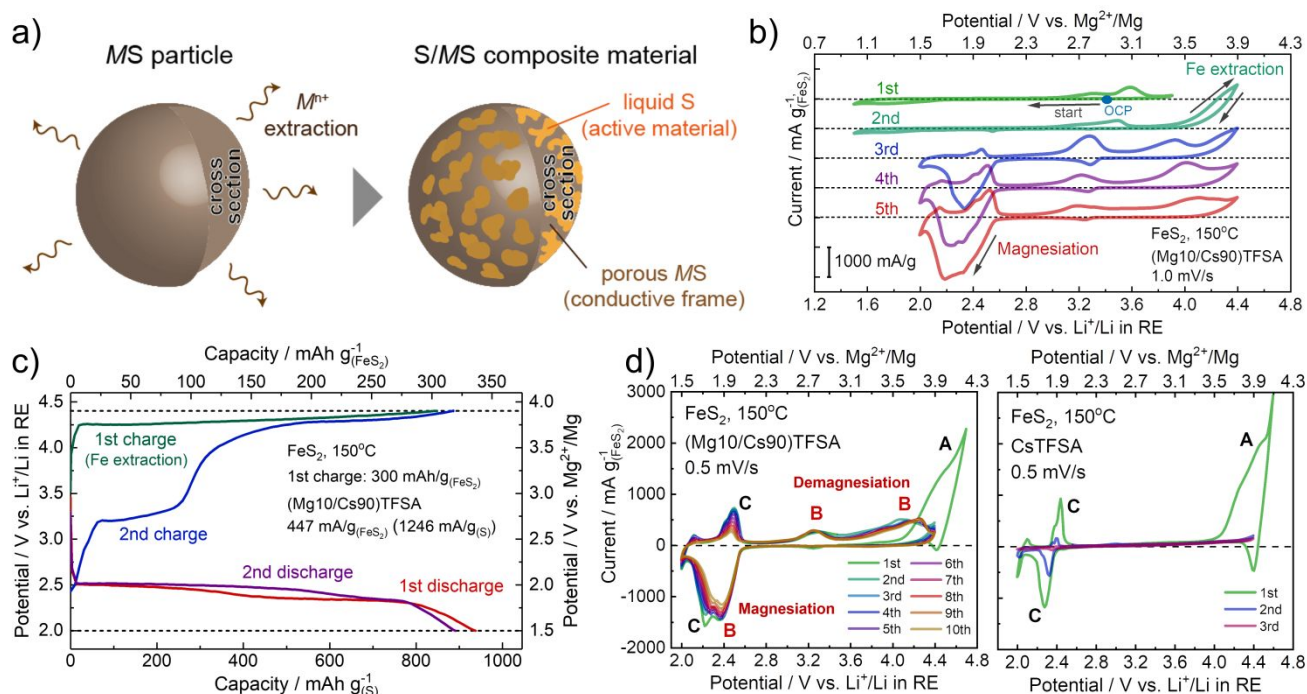

Fig. 1 (a) Schematic illustration and (b) CVs showing the concept of electrochemical synthesis of S/*M*S (*M*S: metal sulfide) composite cathode materials. CV measurements were performed using (Mg10/Cs90)TFSA electrolyte at 150°C, where the first scan was started with an anodic scan from the open circuit potential (OCP). (c) Charge/discharge curves of the S/FeS$_2$ cathode in (Mg10/Cs90)TFSA electrolyte at 150°C. CVs for the S/FeS$_2$ cathode in the electrolytes of (Mg10/Cs90)TFSA (left) and CsTFSA (right) at 150°C, where the redox reactions indicated by B correspond to the magnesiation/demagnesiation of S.

[8–10,13], so it is reliable to work well. The redox potential of Mg^{2+}/Mg is approximately 0.5 V vs. Li RE in this configuration based on our previous study [8]. We should note that it is a rough estimation; it can vary in 0.5–0.6 V vs. Li RE depending on the details of the electrolyte. In this experimental setup, the reversible deposition/dissolution of Cs occurs on the counter electrode [8,9], which enables electrochemical measurements for evaluating cathode materials with suppressing electrolyte decomposition.

Figure 1b shows cyclic voltammograms (CVs) of the FeS_2 cathode at 150°C. The potential range in the first cycle was limited within 1.7–3.9 V vs. Li RE, where Fe^{2+} is hardly extracted from FeS_2. Relatively small redox currents probably due to the conversion reaction of FeS_2 [42] were still observed. The observed capacity was ~40 mAh/$g_{(FeS2)}$, which is much smaller than the theoretical capacity of the conversion reactions (e.g., 894 mAh/$g_{(FeS2)}$ for $FeS_2 + 2Mg^{2+} + 4e \rightarrow Fe + 2MgS$), suggesting that only the surface of the FeS_2 particles electrochemically reacted. Then, the anodic potential limit was expanded to 4.4 V vs. Li RE in the second cycle, which allows Fe to leach from FeS_2. A large oxidative current was observed at ~4.4 V vs. Li RE in the anodic scan, followed by a large reductive current at ~2.4 V vs. Li RE in the subsequent cathodic scan. After that, the anodic and cathodic current peaks were repeatedly observed, indicating the reversible redox reactions. The CV profiles after the Fe^{2+} extraction is in good agreement with those of elemental S with Mg in previous reports [15,21]. Therefore, the major reactions presented here are deduced as follows:

$$FeS_2 \rightarrow x\,(Fe^{2+} + 2\,e) + 2x\,S + (1-x)\,FeS_2 \quad (1)$$
$$S + y\,(Mg^{2+} + 2\,e) \Leftrightarrow Mg_yS \quad (2)$$
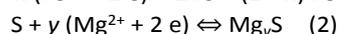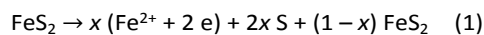
Equivalent redox reactions were observed also in a galvanostatic charge/discharge test (see Figure 1c). The first charge capacity of 300 mAh/$g_{(FeS2)}$ corresponds to the nominal composition of ~$Fe_{0.33}S_2$ (i.e., 0.33 FeS_2 and 1.34 S) when assuming eq 1. The capacity based on elemental S generated in the first charge was also shown on the bottom axis in accordance with eq 2. Notably, the discharge capacities of ~900 mAh/$g_{(S)}$ (~320 mAh/$g_{(FeS2)}$) was achieved at a high current density of 1246 mAh/$g_{(S)}$ (447 mAh/$g_{(FeS2)}$). Furthermore, when doubling the current density to 2492 mA/$g_{(S)}$ (894 mAh/$g_{(FeS2)}$), the discharge capacity of ~550 mAh/$g_{(S)}$ (~200 mAh/$g_{(FeS2)}$) was still retained (Figure S4). Because we have to consider the amounts not only of elemental S but also of the FeS_2 frame in practical use, increasing the molar ratio of S/FeS_2 would be critical for improving the energy density of batteries. However, if the performance is compared based on the active S, the rate capability achieved in this work is more than two times higher than the previously reported highest rate capability of ~500 mAh/$g_{(S)}$ at ~500 mA/$g_{(S)}$ [21,27]. Such a high-rate capability is attributed to the liquid-state reaction; thus, we note that it might not be simply compared with conventional solid materials at room temperature. The obtained capacity for the high-rate discharging process in Figure 1c is approximately half the theoretical value of S/MgS two-phase reaction, i.e., 1672 mAh/$g_{(S)}$. This indicates that metastable solid-state MgS_n ($n \sim 2$) [15,20,22] would be formed during discharge; otherwise, such a fast discharge process could have been completed up to the

full capacity. The discharge capacity reached ~1400 mAh/$g_{(S)}$ when the current density was decreased stepwise from 300 to 5 mA/$g_{(FeS2)}$ (Figure S5), which signifies that the liquid S dries up, thereby eventually causing the decrease in the reaction kinetics. Actually, the galvanostatic intermittent titration technique (GITT) experiment (Figure S6) showed a large overpotential of ~1 V due to the sluggish Mg^{2+} diffusion in such a solid-state phase, which is in contrast to the high-rate liquid state reaction in the early stage of discharge. The theoretical capacity based on the sum of the masses/volumes of active S and remained FeS_2 as a function of the first charge capacity (i.e., the amount of Fe extracted from FeS_2) is summarized in Figure S7.

We compared the CVs obtained in the electrolytes with and without Mg^{2+} ion, namely, (Mg10/Cs90)TFSA and pure CsTFSA, to clarify the electrochemically reacting elements (Figure 1d). Reaction A indicated in CVs was observed in both electrolytes, attributed to the Fe^{2+} extraction from FeS_2. Reaction B was observed only for the measurement in (Mg10/Cs90)TFSA, indicating the magnesiation/demagnesiation of elemental S generated by the oxidation of FeS_2. On the contrary, reaction C can be attributed to the reactions of S with Cs because it was observed in both electrolytes. Indeed, Cs was detected by EDX analysis for the electrode after discharged in pure CsTFSA electrolyte, and a halo peak indicating the formation of an amorphous phase was observed in the XRD profile (FigureS8). The higher potential for the cathodic reaction of B rather than that of C suggests that Mg preferentially reacts with S especially in galvanostatic discharge, as confirmed by the following inductively coupled plasma (ICP) analysis of a discharged sample. Incidentally, the efficiency of discharge/charge is seemingly low because the reduction peak is sharp while the oxidation peaks are broad, but it is actually near 100% (Figure S9).

ICP analysis was carried out firstly for a charged electrode rinsed with water. The amount of S was comparable to that of the pristine electrode, whereas Fe drastically decreased after the charge (Figure S10, sample 2). In contrast, when using triglyme (G3) for washing the electrodes, which dissolves elemental S unlike water, the amounts of Fe and S decreased with keeping the molar ratio of Fe/S at 1/2 (Figure S10, sample 3,4), because the unreacted FeS_2 remained on the electrode. Thus, the above results strongly indicate that Fe was extracted from FeS_2 by the two-phase separation of S and FeS_2 in accordance with eq 1. The amount of remained FeS_2 matches well with the theoretical value assuming eq 1 (see the right panel in Figure S10), indicating high coulombic efficiency. In other words, side reactions such as the oxidation of Fe^{2+} ions are not substantially involved in the first charging process. The XRD profiles for the charged electrodes also support it in that the intensity of diffraction peaks from FeS_2 was ideally lowered by charging (Figure S11). Therefore, we can determine the amount of elemental S according to eq 1. G3 rather than water was used to rinse the discharged electrode for the ICP analysis, because water reacts with the discharged materials (Figure S12). Mg was substantially detected but Cs was remarkably low (Cs/Mg was ~0.03 in molar ratio) for the discharged sample,

ensuring that the contribution of Cs is negligible in the

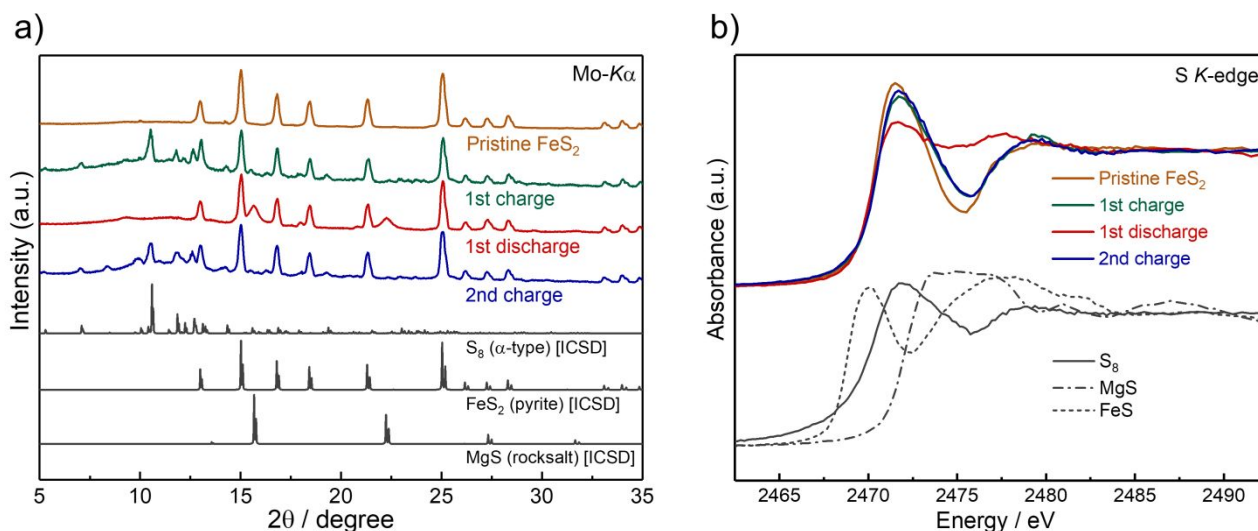The microstructures of the electrodes were analyzed by

Fig. 2 (a) XRD and (b) XANES spectra of the S/FeS$_2$ cathodes after charge/discharge, together with those of standard samples for comparison. The first charge corresponds to the Fe^{2+} extraction from the pristine FeS$_2$. The charged and discharged electrodes were washed with water and G3, respectively.

galvanostatic experiments in (Mg10/Cs90)TFSA.

Figure 2a displays X-ray diffraction (XRD) profiles of the S/FeS$_2$ composite electrodes, whose charge/discharge curves are shown in Figure S13. The charged and discharged electrodes were washed with water and G3, respectively. Note that the intensities of the profiles were normalized by the highest peaks. The first charged electrode clearly showed the coexistence of crystalline S$_8$ and remained FeS$_2$, which is consistent with the ICP results and eq 1. As for the discharged electrode, broad diffraction peaks of crystalline MgS with the rocksalt structure were observed. Although a metastable MgS$_n$ ($n \sim$ 2) phase would form during discharge, it can disproportionate into equilibrium phases (i.e., S$_8$ and MgS) before performing the *ex-situ* XRD measurement. S$_8$ was absent in the discharged electrode because it is removed in washing with G3. The XRD profile of the second charged electrode is coincident with that of the first charged electrode, indicating high reversibility in charge/discharge.

X-ray absorption near-edge structures (XANES) were measured for the charged/discharged electrodes. The valence state of Fe remained 2+ during charge/discharge in that XANES spectra at Fe K-edge show no obvious change (Figure S14). On the other hand, XANES spectra at S K-edge varied after charge/discharge as shown in Figure 2b. The absorbance at around 2474 eV slightly increased after the first charge while the edge energy at ~2470 eV hardly changed, suggesting that the elemental S was formed to coexist with FeS$_2$. The large increase in absorbance at ~2476 eV after the first discharge is attributed to the formation of MgS. The XANES of the second charged electrode was coincident with that of the first charged electrode, indicating that the solid-state MgS$_n$ ($n \sim$ 2) formed in discharge favorably reverted to elemental S in the subsequent charge process as also observed in XRD results.

focused ion beam scanning electron microscopy (FIB-SEM) to morphologically reveal the reaction mechanism (see Figure 3a). The cross-sections of the pristine (Figure 3b) and first charged (Figure 3c) electrodes washed with G3 indicate that a porous structure was formed in a coarse particle after charging. This suggests that Fe was heterogeneously extracted from the FeS$_2$ matrix to form a hollow structure inside the particle with keeping the apparent particle shape. This is similar to the dealloying method for fabricating porous materials used in our previous work [43]. Figures 3d–h show SEM and corresponding energy-dispersive X-ray (EDX) mapping images for the discharged electrode. It was clearly seen that Mg reacted with S existing in the pores of FeS$_2$ frame, which was also shown by the SEM-EDX observations of electrodes without the FIB milling (Figure S15). Because Fe extraction occurs from the surface of FeS$_2$ particles, smaller particle size would be advantageous in terms of the utility of FeS$_2$. In fact, the current density in CVs for FeS$_2$ particle was significantly improved after removing the large particles by filtering (Figure S16).

In addition, it was experimentally clarified that a droplet of liquid S was immiscible in the electrolyte of (Mg10/Cs90)TFSA (Figure S17a,b) while it showed excellent wettability to the FeS$_2$ electrode (Figure S17c,d). Besides, cross-sectional SEM-EDX for the electrode after the first charging process showed that elemental S was retained inside and around the FeS$_2$ porous frame (Figure S18). These results indicate that the liquid S generated in the first charge was not released to the electrolyte but attracted to the FeS$_2$ frame. Indeed, the cyclability depends on the microstructure of S/FeS$_2$ cathode. When charging to the theoretical capacity of 447 mAh/g$_{(FeS2)}$ in the first oxidation process to fully extract Fe^{2+} ions from FeS$_2$, a rapid capacity fading was observed (see Figure S19a) due to the absence of the FeS$_2$ frame for retaining liquid S in it. This result was also
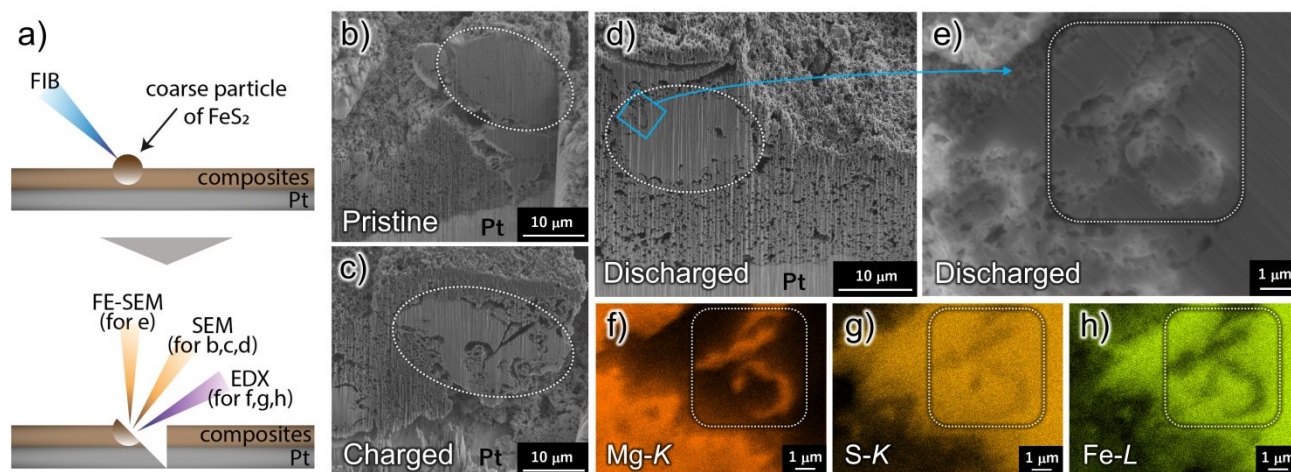
Fig. 3 (a) Schematic illustration showing the procedure of FIB-SEM observation. The composite electrodes were cut at a 45-degree angle by FIB milling and then SEM images were obtained. The cross-section images for the (b) pristine, (c) charged, and (d) discharged electrodes. (e) FE-SEM image of the discharged electrode, which is an enlarged view of the area indicated by a blue rectangle in (d). The corresponding EDX mappings for (f) Mg, (g) S, and (h) Fe elements. All samples were washed with G3 to observe the morphology of FeS_2 frame.

supported by the fact that a conventional cathode of elemental S with carbon and binder (without FeS_2) exhibited a poor cyclability (Figure S20). In contrast, the cyclability was greatly improved by decreasing the first charge capacity to 223 mAh/$g_{(FeS2)}$, i.e., the nominal composition of $Fe_{0.5}S_2$ after the Fe^{2+} extraction (Figure S19b). The FeS_2 frame, therefore, plays an important role in anchoring S and eventually improving the cyclability. Proper choice of the electrolyte is also important for lowering the dissolution of S-based species. To decrease the dissolubility of such soft anions, selecting hard cations (e.g., alkali metals) would be effective. Thus, the (Mg10/Cs90)TFSA ionic liquid electrolyte is suitable for evaluating the S/sulfide cathode materials. Conversely, relatively soft onium cations, for example, would not be suitable. Besides, it was reported that the solubility of LiS_x is much higher than that of MgS_x by approximately two orders [22]. In fact, when we used an ionic liquid consisting of LiTFSA and N2222-TFSA as the electrolyte, the S/FeS_2 cathode showed a rapid capacity fading (Figure S21). In addition to the cation selection, we found that the cyclability can be relatively improved by decreasing the operating temperature (Figure S22) and increasing the composition of Mg(TFSA)$_2$ in the electrolyte (Figure S23), both of which would contribute to suppressing the dissolution of S and/or polysulfides.

Next, we discuss the detailed charge/discharge mechanisms. Multiple plateaus appeared at ~3.2 and ~4.2 V vs. Li RE during second charge (Figure 1c), suggesting the formation of an intermediate phase. Actually, the presence of a longer-chain polysulfide was indicated by the observation that water, which hardly dissolves elemental S and MgS_2, was colored yellow in rinsing an intermediately charged electrode (Figure S24). Actually, the diffraction peaks of S_8, which should appear when not considering the intermediate species, were absent in the XRD profile (Figure S25a). Each capacity of the plateaus in the second charge was estimated to be ~400 mAh/$g_{(S)}$ as seen in Figure 1c, which is approximately half of the first discharge

capacity. Hence, MgS_4 is the most plausible intermediate state, judging from the theoretical capacity (i.e., 418 mAh/$g_{(S)}$ for 1/4 $MgS_4 \rightarrow$ 1/4 Mg^{2+} + 1/2 e + S). It was, however, quite challenging to directly detect the intermediate polysulfide by *ex-situ* experiments of XRD, XANES, and Raman spectroscopy (see Figures S25,S26), because it would be easily disproportionate to the other species such as MgS and elemental S.

Interestingly, when discharging 10 min after a high-rate charging process (i.e., 1000 mA/$g_{(FeS2)}$), a plateau at as high as ~3.3 V vs. Li RE, appeared as shown in Figure 4a. It was revealed by EDX analysis that this high-potential plateau is derived from the reaction with Mg (Figure S27). Besides, a similar reaction was also observed in a high-rate CV measurement (Figure S28). The discharge plateau at ~3.3 V vs. Li RE disappeared by resting for 60 min after the charging process (Figure 4a, lower panel); therefore, the high-potential plateau can be attributed to a non-equilibrium reaction. S exists in different forms in the materials such that the S_8 molecule is a stable structure in liquid S while S–S dumbbell exists in the pyrite structure of FeS_2. Thus, it is expected that non-equilibrium species such as short-chain S molecules [44] were temporally yielded before forming the complete S_8 molecule immediately after the extraction of Fe^{2+} from FeS_2 (see Figure 4b). In addition, the porous sulfide host would play a role in absorbing them on the surface because it has a high affinity with S-based compounds [31–33], which is a characteristic point compared to the carbon host. Such non-equilibrium species should have the Gibbs free energy higher than that of stable S_8 molecules. This results in the higher discharge potential even if the same Mg–S compound, for example, MgS_2, is formed during discharge (see Figure 4c), because the difference in the chemical potentials of Mg between the anode and cathode is proportional to the electromotive force (*emf*). In a similar manner, relatively high potentials in the later stage of the charging process can be explained by the formation of non-equilibrium S during the charging process. The increase in the chemical potential of S can
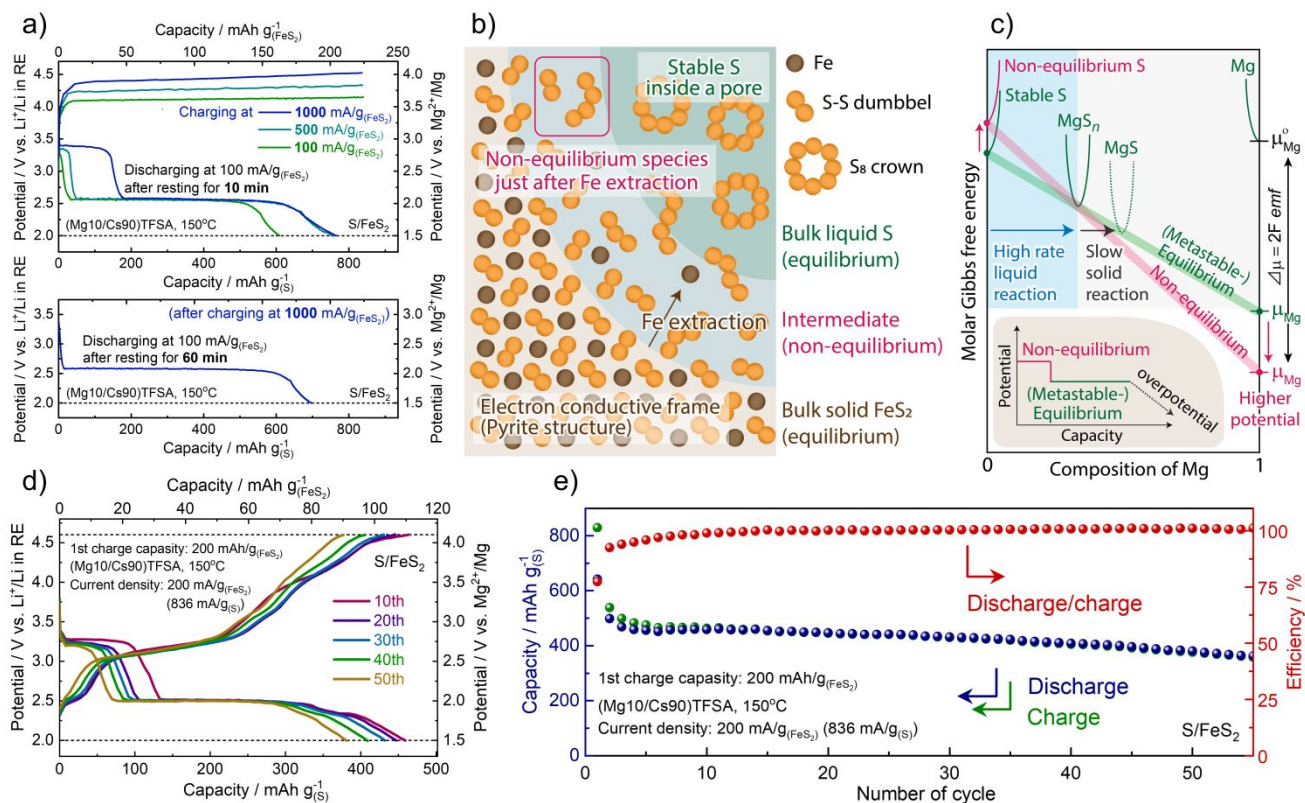
Fig. 4 (a) Galvanostatic charge/discharge performance of the S/FeS$_2$ cathode with PVdF binder. Following the charging process at several different current densities, it was discharged at 100 mA/g$_{(FeS2)}$ after resting for 10 (upper) and 60 (lower) min. (b) Schematic illustration of the expected structure change of S during the charging process. Because S exists as S–S dumbbell in the pyrite structure while the stable structure is S$_8$ in the liquid state at 150°C, non-equilibrium species would exist near the surface of the FeS$_2$ frame just after the extraction of Fe^{2+} from FeS$_2$. (c) Schematic chemical-potential diagram for explaining the change in discharge potentials for the non-equilibrium S having a relatively higher chemical potential just after the charging process. The inset shows the predicted potential-change behavior during discharge from equilibrium (green) and non-equilibrium (pink) S. (d,e) Charge/discharge performance of the S/FeS$_2$ cathode with PTFE binder in the (Mg10/Cs90)TFSA at 150°C. The subsequent discharge/charge cycling test was conducted at 200 mA/g$_{(FeS2)}$, i.e., 836 mA/g$_{(S)}$.

also induce the formation of intermediate species as shown in Figure S29. This could be the reason that a two-step reaction was observed in the charging process but not in discharging process when there are enough rest times for the relaxation of non-equilibrium S (e.g., Figure 1c and 1d). As for the equilibrium discharge process, the potential is still slightly higher than the thermodynamically predicted value (i.e., 1.77 V vs. Mg^{2+}/Mg). This indicates that the stabilities of S and/or Mg-S compounds are influenced by the environment in the cell. Specifically, S dispersed in porous FeS$_2$ with ionic liquid electrolyte is different from the condition of bulk S$_8$ phase, which can lead to the increase in the Gibbs free energy even after waiting time. In addition, Mg-S compounds are possibly stabilized by the interaction with the electrolyte. In fact, a discharge potential of as high as 2.5 V vs. Mg^{2+}/Mg due to the formation of a polysulfide was reported in previous literature [22]. Therefore, we referred to as (metastable-) equilibrium in the figure.

We also found that the high potential discharge reaction was stably obtained by changing the binder of the electrode from PVdF to polytetrafluoroethylene (PTFE) as shown in Figure 4d. PTFE would be a better choice due to its high thermal stability. In addition, no need for solvents in preparing the

electrode is suitable for preventing the oxidation of FeS$_2$. In contrast, unstable behavior was obtained when using CMC binder (Figure S30), because it needs water solvent in preparing the electrode and shows lower thermal stability. Long-term cyclability including the high potential discharge plateau was successfully demonstrated, keeping the total capacity of ~380 mAh/g$_{(S)}$ even after 50 cycles with the coulombic efficiency of almost 100% (Figure 4e). The capacity fading was still slightly observed, whereas the specific cause is unclear. Although the parasitic reactions in the electrolyte (e.g., decomposition of TFSA, redox reactions derived from Fe^{2+} ions) should also be considered, we suppose that the dissolution of S into the electrolyte is a major problem because it is not completely inhibited even using the ionic liquid electrolyte especially in beaker-type cells (Figure S31). Besides, a part of dissolved S would evaporate and be released from the electrochemical system. In order to assess it, we performed charge/discharge tests with and without a S droplet for saturating the electrolyte (Figure S32). As expected, the discharge capacity was enhanced in the cell with a S droplet. However, such a problem would be prevented in practical batteries because they are basically closed systems.

In this work we used a beaker-type cell with a sufficient amount of electrolyte for preventing parasitic reactions of Fe^{2+} ions extracted from FeS_2. Although the electrolytes after electrochemical measurements colored brown because of the dissolution of Fe^{2+} ions (Figure S33), Fe was not detected by EDX analysis on the Mg counter electrode after a charging process. This is probably due to the difficulties of Fe deposition from the ionic liquid electrolyte as well as its low concentration (i.e., the molar ratio of Mg/Fe is over 200 in the electrolyte). In practical use, S/FeS_2 composite materials should be prepared in advance for preventing the contamination of Fe^{2+} ions in the electrolyte. Thus, we examined the electrochemical behavior of a S/FeS_2 composite electrode prepared in CsTFSA electrolyte before the CV measurement in (Mg10/Cs90)TFSA. The obtained CV profiles (Figure S34) are very similar to the in-situ synthesized samples (e.g., Figure 1d), indicating that the effect of Fe^{2+} contamination on the cathode performance is negligible. A big challenge for achieving practical batteries is that there are few electrolytes compatible with both cathode and anode materials. We tried to construct a prototype cell consisting of the S/FeS_2 cathode and Mg-metal anode by using a highly concentrated $Mg(TFSA)_2$–$MgCl_2$/G3 electrolyte [41], which shows sufficient high thermal stability with suppressing the passivation of Mg-metal anode. However, a rapid capacity fading was observed (Figure S35), probably due to the dissolution of S into the G3-based electrolyte. Although it is a general problem in the field of MRBs, the development of advanced electrolytes would be required to realize full-cell MRBs.

The versatility of the present concept was examined using other metal sulfides. The cathode performance of CoS_2 with the pyrite structure (Figure S36) was basically similar to that of FeS_2. The reaction kinetics would be slightly improved, presumably due to the better electronic conductivity of CoS_2 having a half-metallic electronic structure [31]. In addition, TiS_2, which has a layered structure with high electronic conductivity, showed similar behavior to the sulfides with the pyrite structure (Figure S37a). In contrast, such attractive behavior was not observed when using FeS, MgS, and MoS_2 as the starting materials (Figures S37b–d). Although FeS has a narrow band gap [45], the molar ratio of S/cation in FeS and MgS is lower than those in the aforementioned pyrite and layered structure materials, which would be disadvantageous for generating elemental S by the cation extraction from sulfides. On the other hand, even though MoS_2 has a layered structure like TiS_2, the extraction of 4d transition metals is expected to be difficult because of their relatively high covalency with S. Therefore, as far as the sulfides we examined, the criteria for the starting material of our method could be summarized as follows: (i) The sulfide should have high electronic conductivity. (ii) The higher molar ratio of S/cation in the sulfide would be better. (iii) 4d transition metals would not be suitable for the cation to be extracted from the sulfide.

Finally, we assessed the feasibility of using the S/FeS_2 composite material as the cathode for Li–Mg dual-cation batteries, which have recently attracted increasing attention [46–48]. As shown in Figure S38, redox reactions associated with both Li and Mg were clearly observed, indicating that our approach is also promising for the dual-cation battery system. We believe that such a great versatility in the selection of starting materials and carrier ions accelerates the development of next-generation rechargeable batteries.

Conclusions

In conclusion, we have demonstrated the feasibility of the electrochemically synthesized S/FeS_2 composite cathode materials enabling high-rate MRBs. By the electrochemical oxidation of FeS_2 in an ionic liquid electrolyte at 150°C, Fe^{2+} cations are extracted from FeS_2 to generate elemental S as a separated phase. A porous structure is formed inside the FeS_2 particles by Fe^{2+} extraction in the first charge, filled with the generated liquid S, which eventually reacts with Mg during the subsequent cycling. Although the limited amount of active S is disadvantageous in terms of energy density, attractive rate capabilities of, e.g., ~900 mAh/$g_{(S)}$ at 1246 mA/$g_{(S)}$ based on the mass of active S is achieved for the S/FeS_2 composite material owing to the liquid state reactions. It also exhibits markedly stable cyclabilities due to the high structural reversibility in charge/discharge, which is elucidated by *ex-situ* XRD and XANES analyses. In addition, we have discussed the mechanism for enhancing the discharge potential of S cathode by utilizing non-equilibrium species formed by the fast-charging process. This work would provide a new option for the development of Mg-S batteries that face challenges for exploiting solid S cathode.

Experimental

Materials preparation

Commercial FeS_2 powder (99.9%, Furuuchi Chemical) was used for the electrochemical measurements. The FeS_2 powder was filtered before preparing the electrodes to eliminate large particles above ~100μm. We also synthesized FeS_2 powder for the FIB-SEM, XRD, and ICP analyses by the following procedure. The mixture of Fe (99.9%, Kojundo Chemical Laboratory) and S (99.99%, Kojundo Chemical Laboratory) powders was pelletized and then encapsulated in a quartz ampoule with Ar gas. The heat treatment was carried out at 420°C for 24 hours. The obtained material was hand-milled in a glove box under an Ar atmosphere. We have confirmed by XRD that a fine FeS_2 powder was successfully synthesized.

Electrochemical measurements

Electrochemical measurements were carried out using a galvanostat/potentiostat (Biologic, VMP-3). Three-electrode beaker-type cell (see Figure S3) was constructed in a glove box filled with Ar gas. Eectrodes were prepared by mixing FeS_2, carbon black (super C65), and PVdF binder in a weight ratio of 80:10:10 and then coating it on a Pt foil, which is denoted as the pristine FeS_2 electrode in the main text. The mass loading of FeS_2 was approximately 2 mg/cm². We also prepared composite electrodes with a mixture of FeS_2, carbon black, PTFE binder in a weight ratio of 70:25:5 pressed on an Al-mesh current collector. Mg metal used for the counter electrode was polished

with sandpaper prior to use. Li metal immersed in the solution of 0.5 M LiTFSA/DEME-TFSA (DEME: N,N-diethyl-N-methyl-N-(2-methoxyethyl)ammonium) was used for the reference electrode (denoted as Li RE). LiTFSA (Kishida Chemical) and DEME-TFSA (Kanto Chemical) were used for preparing the 0.5 M LiTFSA/DEME-TFSA solution. (Mg10/Cs90)TFSA ionic liquid electrolyte was prepared by mixing $Mg(TFSA)_2$ (battery grade, Kishida Chemical) and CsTFSA (battery grade, Morita Chemical Industry) at 150°C for several days in a glove box. The redox potential of Mg^{2+}/Mg in the (Mg10/Cs90)TFSA electrolyte was estimated to be ~0.5 V vs. Li RE in our previous report [8]. The electrochemical window of the electrolyte was also previously evaluated to be ~5 V vs. Li RE [8,9]. Typically, 2.5 ml of the electrolyte was used for each electrochemical cell.

Electrode characterization

Electrode samples after electrochemical measurements were rinsed with triglyme (G3) or water, where G3 solvent (99%, Tokyo Chemical Industry) was treated with 3A molecular sieves prior to use. The residual G3 solvent on the electrode was removed by soaking in dimethyl carbonate. XRD measurements were performed by using an X-ray diffractometer (Rigaku, SmartLab) with Mo-*K*α radiation. Each composite sample was enclosed in a glass capillary and measured in a transmission geometry at room temperature. Fluorescence XANES experiments were carried out at BL5S1 and BL6N1 of Aichi Synchrotron Radiation Center (AichiSR). The electrodes were sealed in a laminated Al film under an Ar atmosphere for the measurements at Fe *K*-edge. Then, they were transferred to a vessel in a glove box for the measurements at S *K*-edge. MgS (99.9%, Kojundo Chemical Laboratory), S (99.99%, Kojundo Chemical Laboratory), and FeS (99.9%, Alfa Aesar) powders were used for the standard samples. The obtained data were analyzed using the Athena program [49]. Cross-sectional SEM images were obtained by using a focused ion beam equipment (Hitachi, SMI3050SE). The electrodes were transferred to a field-emission scanning electron microscope (JEOL, JSM-7200F) to obtain SEM-EDX mapping images. EDX mapping for a discharged sample without FIB milling was conducted using a scanning electron microscope (JEOL, JSM-IT200). Raman spectra were obtained by using a Raman microscope (JASCO, NRS-5100) with an exciting laser of 532 nm at room temperature. CoS_2 (99.98%, Sigma-Aldrich) and MoS_2 (99%, Sigma-Aldrich) powders were also used for electrochemical experiments.

Author Contributions

K.S. conceived the idea of this study, and T.I. supervised the project. K.S. and T.F. conducted the sample preparation, electrochemical measurements, and electrode characterization. T.K., T.F., and K.S. carried out the experiment and analysis of XANES. W.-Y. P., T.W., and H.K. conducted the FIB-SEM observation. H.M. prepared Li-based ionic liquid electrolytes for electrochemical measurements. K.S., T.K., and T.I. wrote the manuscript. All authors discussed the results and commented on the manuscript.

Conflicts of interest

There are no conflicts to declare.

Acknowledgements

References

1 J. Muldoon, C. B. Bucur, T. Gregory, *Chem. Rev.*, 2014, **114**, 11683–11720.
2 D. Aurbach, Y. Cohen, M. Moshkovich, *Electrochem. Solid-State Lett.*, 2001, **4**, A113–A116.
3 M. Matsui, *J. Power Sources*, 2011, **196**, 7048–7055.
4 D. Aurbach, Z. Lu, A. Schechter, Y. Gofer, H. Gizbar, R. Turgeman, Y. Cohen, M. Moshkovich, E. Levi, *Nature*, 2000, **407**, 724–727.
5 T. Koketsu, J. Ma, B. J. Morgan, M. Body, C. Legein, W. Dachraoui, M. Giannini, A. Demortière, M. Salanne, F. Dardoize, H. Groult, O. J. Borkiewicz, K. W. Chapman, P. Strasser, D. Dambournet. *Nat. Mater.*, 2017, **16**, 1142–1148.
6 X. Sun, P. Bonnick, V. Duffort, M. Liu, Z. Rong, K. A. Persson, G. Ceder, L. F. Nazar, *Energy Environ. Sci.*, 2016, **9**, 2273–2277.
7 Y. Sun, Q. Zou, Y.-C. Lu, *Adv. Energy Mater.* 2019, **9**, 1903002.
8 S. Okamoto, T. Ichitsubo, T. Kawaguchi, Y. Kumagai, F. Oba, S. Yagi, K. Shimokawa, N. Goto, T. Doi, E. Matsubara, *Adv. Sci.*, 2015, **2**, 1500072.
9 K. Shimokawa, T. Atsumi, M. Harada, R. E. Ward, M. Nakayama, Y. Kumagai, F. Oba, N. L. Okamoto, K. Kanamura, T. Ichitsubo, *J. Mater. Chem. A*, 2019, **7**, 12225–12235.
10 T. Hatakeyama, N. L. Okamoto, K. Shimokawa, H. Li, A. Nakao, Y. Uchimoto, H. Tanimura, T. Kawaguchi, T. Ichitsubo, *Phys. Chem. Chem. Phys.*, 2019, **21**, 23749–23757.
11 N. L. Okamoto, K. Shimokawa, H. Tanimura, T. Ichitsubo, *Scr. Mater.* 2019, **167**, 26–30.
12 K. Shimokawa, T. Ichitsubo, *Curr. Opin. Electrochem.*, 2020, **21**, 93–99.
13 K. Shimokawa, T. Atsumi, N. L. Okamoto, T. Kawaguchi, S. Imashuku, K. Wagatsuma, M. Nakayama, K. Kanamura, T. Ichitsubo, *Adv. Mater.*, 2020, **33**, 2007539.
14 H. S. Kim, T. S. Arthur, G. D. Allred, J. Zajicek, J. G. Newman, A. E. Rodnyansky, A. G. Oliver, W. C. Boggess, J. Muldoon, *Nat. Commun.*, 2011, **2**, 427.
15 Z. Zhao-Karger, X. Zhao, D. Wang, T. Diemant, R. J. Behm, M. Fichtner, *Adv. Energy Mater.*, 2015, **5**, 1401155.
16 T. Gao, M. Noked, A. J. Pearse, E. Gillette, X. Fan, Y. Zhu, C. Luo, L. Suo, M. A. Schroeder, K. Xu, S. B. Lee, G. W. Rubloff, C. Wang, *J. Am. Chem. Soc.*, 2015, **137**, 12388–12393.
17 X. Yu, A. Manthiram, *ACS Energy Lett.*, 2016, **1**, 431–437.
18 B. P. Vinayan, Z. Zhao-Karger, T. Diemant, V. S. K. Chakravadhanula, N. I. Schwarzburger, M. A. Cambaz, R. J. Behm, C. Kübel, M. Fichtner, *Nanoscale*, 2016, **8**, 3296–3306.
19 Z. Zhang, Z. Cui, L. Qiao, J. Guan, H. Xu, X. Wang, P. Hu, H. Du, S. Li, X. Zhou, S. Dong, Z. Liu, G. Cui, L. Chen, *Adv. Energy Mater.*, 2017, **7**, 1602055.
20 A. Robba, A. Vizintin, J. Bitenc, G. Mali, I. Arčon, M. Kavčič, M. Žitnik, K. Bučar, G. Aquilanti, C. Martineau-Corcos, A. Randon-Vitanova, R. Dominko, *Chem. Mater.*, 2017, **29**, 9555–9564.
21 A. Du, Z. Zhang, H. Qu, Z. Cui, L. Qiao, L. Wang, J. Chai, T. Lu, S. Dong, T. Dong, H. Xu, X. Zhou, G. Cui, *Energy Environ. Sci.*, 2017, **10**, 2616–2625.

22 T. Gao, X. Ji, S. Hou, X. Fan, X. Li, C. Yang, F. Han, F. Wang, J. Jiang, K. Xu, C. Wang, *Adv. Mater.*, 2018, **30**, 1704313.

23 Z. Zhao-Karger, R. Liu, W. Dai, Z. Li, T. Diemant, B. P. Vinayan, C. B. Minella, X. Yu, A. Manthiram, R. J. Behm, M. Ruben, M. Fichtner, *ACS Energy Lett.*, 2018, **3**, 2005–2013.

24 X. Zhou, J. Tian, J. Hu, C. Li, *Adv. Mater.*, 2018, **30**, 1704166.

25 Y. Xu, Y. Ye, S. Zhao, J. Feng, J. Li, H. Chen, A. Yang, F. Shi, L. Jia, Y. Wu, X. Yu, P.-A. Glans-Suzuki, Y. Cui, J. Guo, Y. Zhang, *Nano Lett.*, 2019, **19**, 2928–2934.

26 Z. Zhou, B. Chen, T. Fang, Y. Li, Z. Zhou, Q. Wang, J. Zhang, Y. Zhao, *Adv. Energy Mater.*, 2020, **10**, 1902023.

27 D. Huang, S. Tan, M. Li, D. Wang, C. Han, Q. An, L. Mai, *ACS Appl. Mater. Interfaces*, 2020, **12**, 17474–17480.

28 H. Kaland, F. H. Fagerli, J. Hadler-Jacobsen, Z. Zhao-Karger, M. Fichtner, K. Wiik, N. P. Wagner, *ChemSusChem*, 2021, **14**, 1864–1873.

29 Y. Ji, X. Liu-Théato, Y. Xiu, S. Indris, C. Njel, J. Maibach, H. Ehrenberg, M. Fichtner, Z. Zhao-Karger, *Adv. Funct. Mater.*, 2021, 2100868.

30 B. Meyer, *Chem. Rev.*, 1976, **76**, 367–388.

31 Z. Yuan, H.-J. Peng, T.-Z. Hou, J.-Q. Huang, C.-M. Chen, D.-W. Wang, X.-B. Cheng, F. Wei, Q. Zhang, *Nano Lett.*, 2016, **16**, 519–527.

32 Q. Pang, D. Kundu, L. F. Nazar, *Mater. Horiz.* 2016, **3**, 130–136.

33 X. Liu, J.-Q. Huang, Q. Zhang, L. Mai, *Adv. Mater.*, 2017, **29**, 1601759.

34 R. D. McAuliffe, D. P. Shoemaker, *Acta Cryst.*, 2018, **B74**, 436–444.

35 K. Ohara, Y. Umebayashi, T. Ichitsubo, K. Matsumoto, R. Hagiwara, H. Arai, M. Mori, Y. Orikasa, S. Okamoto, M. Oishi, Y. Aiso, T. Nohira, Y. Uchimoto, Z. Ogumi, E. Matsubara, *RSC Adv.*, 2015, **5**, 3063–3069.

36 J.-W. Park, K. Yamauchi, E. Takashima, N. Tachikawa, K. Ueno, K. Dokko, M. Watanabe, *J. Phys. Chem. C*, 2013, **117**, 4431–4440.

37 J.-W. Park, K. Ueno, N. Tachikawa, K. Dokko, M. Watanabe, *J. Phys. Chem. C*, 2013, **117**, 20531–20541.

38 K. Dokko, N. Tachikawa, K. Yamauchi, M. Tsuchiya, A. Yamazaki, E. Takashima, J.-W. Park, K. Ueno, S. Seki, N. Serizawa, M. Watanabe, *J. Electrochem. Soc.*, 2013, **160**, A1304–A1310.

39 M. Oishi, T. Ichitsubo, S. Okamoto, S. Toyoda, E. Matsubara, T. Nohira, R. Hagiwara, *J. Electrochem. Soc.*, 2014, **161**(6) A943–A947.

40 N. N. Rajput, X. Qu, N. Sa, A. K. Burrell, K. A. Persson, *J. Am. Chem. Soc.*, 2015, **137**, 3411–3420.

41 K. Shimokawa, H. Matsumoto, T. Ichitsubo, *J. Phys. Chem. Lett.*, 2018, **9**, 4732–4737.

42 Y. Zhang, J. Xie, Y. Han, C. Li, *Adv. Funct. Mater.*, 2015, **25**, 7300–7308.

43 T. Wada, T. Ichitsubo, K. Yubuta, H. Segawa, H. Yoshida, H. Kato, *Nano Lett.*, 2014, **14**, 4505–4510.

44 S. Xin, L. Gu, N.-H. Zhao, Y.-X. Yin, L.-J. Zhou, Y.-G. Guo, L.-J. Wan, *J. Am. Chem. Soc.*, 2012, **134**, 18510–18513.

45 J. R. Gosselin, M. G. Townsend, R. J. Tremblay, *Solid State Commun.*, 1976, **19**, 799–803.

46 S. Yagi, T. Ichitsubo, Y. Shirai, S. Yanai, T. Doi, K. Murase, E. Matsubara, *J. Mater. Chem. A*, 2014, **2**, 1144–1149.

47 T. Ichitsubo, S. Okamoto, T. Kawaguchi, Y. Kumagai, F. Oba, S. Yagi, N. Goto, T. Doi, E. Matsubara, *J. Mater. Chem. A*, 2015, **3**, 10188–10194.

48 H. Li, N. L. Okamoto, T. Hatakeyama, Y. Kumagai, F. Oba, T. Ichitsubo, *Adv. Energy Mater.*, 2018, **8**, 1801475.

49 B. Ravel, M. Newville, *J. Synchrotron Rad.*, 2005, **12**, 537–541.